

Article

## Design Considerations for Wireless Charging Systems with an Analysis of Batteries

Zhenshi Wang <sup>1,2</sup> and Xuezhe Wei <sup>2,\*</sup>

<sup>1</sup> Clean Energy Automotive Engineering Center, Tongji University, Shanghai 201804, China; E-Mail: 1022wangzhenshi@tongji.edu.cn

<sup>2</sup> College of Automotive Studies, Tongji University, Shanghai 201804, China

\* Author to whom correspondence should be addressed; E-Mail: weixzh@tongji.edu.cn; Tel.: +86-21-6958-3764; Fax: +86-21-6958-9121.

Academic Editor: K. T. Chau

Received: 31 July 2015 / Accepted: 22 September 2015 / Published: 25 September 2015

---

**Abstract:** Three criteria, including charging time, effective charging capacity and charging energy efficiency, are introduced to evaluate the CC (constant current) and CC/CV (constant current/constant voltage) charging strategies. Because the CC strategy presents a better performance and most resonant topologies have the CC characteristic, the CC strategy is more suitable for the design of wireless charging systems than the CC/CV strategy. Then, the state space model of the receiver is built to study the system dynamic characteristics, and the design of nonuse output filter capacitors is proposed, which can improve the system power density and avoid the drop in efficiency caused by capacitor degradation. At last, an electrochemical impedance spectrum (EIS) based analysis method is introduced to validate that the design without output filter capacitors has no effects on the battery characteristics when the charging frequency is higher than 460 Hz. A prototype is fabricated to verify our research results.

**Keywords:** wireless charging system; charging strategy; state space model; EIS

---

### 1. Introduction

Wireless power transfer is becoming more and more popular in our daily life. It is widely used in medical implantation [1,2], industrial and consumer electronics [3], and wireless sensor networks [4],

and it is particularly suitable for vehicular power battery charging as it can remove the troublesome plug-in process, provide an inherent electrical isolation and adapt to harsh environments [5]. The wireless power transfer technique discussed in this paper is based on electromagnetic induction, which conforms to Faraday's and Ampere's laws [6]. Other wireless power transfer methods, like the capacitively coupled power transfer, are not considered. The issues of concern include principle elaboration [7], impedance matching [8], frequency splitting [9], system architecture [10], circuit topology [11], coil optimization [12], magnetic structure design [13], dynamic online charging [14] as well as power control and efficiency analysis [15,16]. Recently, metamaterial has become a new hot spot in wireless power transfer systems [17,18], which acts as a "superlens" to increase the mutual inductance, and hence, the transfer efficiency.

Up to now, the design of wireless charging systems for electric vehicles has not paid attention to battery characteristics; thus, this paper aims to put forward some design considerations for wireless charging systems with an analysis of batteries. CC/CV (constant-current/constant-voltage) is a traditional charging strategy which is initially used to charge the lead-acid battery. However, the lead-acid battery is usually replaced by the lithium-ion battery in practice, for the latter has high energy and power density [19]. As the lithium-ion battery characteristics are obviously different from those of the lead-acid battery [20,21], the CC/CV strategy may be not the best charging technique for the lithium-ion battery. So, a comparison between CC (constant current) strategy and CC/CV strategy is made based on three criteria which include the charging time, the charging capacity and the charging energy efficiency. The results indicate that a CC strategy is better than a CC/CV strategy. Additionally, a CC strategy is easier to be implemented in wireless charging systems, for most resonant topologies have the CC characteristic. Dynamic characteristics are very important for online control, however, the analysis method based on laplace phasor transform is a little complicated [22]. Instead, a state space model is built to study the systematic characteristics in this paper, and we further propose a new design without the output filter capacitors to reduce the volume and weight of the receiver. An electrochemical impedance spectrum (EIS) based analysis method is employed to study whether the design without output filter capacitors has negative effects on the battery characteristics, since EIS curve corresponds to the internal polarization processes of the battery, which can describe the electrochemical mechanism of the battery. At last, a prototype is achieved to validate our research results.

## 2. Wireless Charging Strategy

Topologies are very important for wireless charging systems, for they are the major power transfer carrier and affect the system transfer characteristics. LC series and LC parallel are the basic two topologies, and their combinations derive four topologies, including LC series-LC series, LC series-LC parallel, LC parallel-LC series and LC parallel-LC parallel [23]. To ensure the reflected impedance of LC parallel topology is purely resistive, an additional inductor is employed to compensate the imaginary part, which derives the LCL-LCL topology [11]. According to the Norton's law, we can easily deduce that the LC parallel topology and LCL topology have the CC characteristic [24]. Additionally, LC series-LC series topology also has a CC characteristic when the load is a strong voltage source, like the battery. So, we can use these topologies to charge the battery directly, which can remove the cascade DC/DC part in the receiver, and thus improve the efficiency. CC/CV strategy is widely used due to the

requirements of many commercial power batteries [25]. The battery is at first charged by a constant current. Once its terminal voltage arrives at a predesigned value, the CV stage begins. At this time, the charging instrument works as a voltage source to clamp the terminal voltage of the battery. Then, the internal resistance and OCV (open circuit voltage) of the battery increase continually until the charging current reduces to a threshold, which indicates that the charging process is over. Obviously, we can find that the CC stage is realized easily in wireless charging systems, but for the CV stage, it needs an additional control algorithm as well as some other sensors at high speed [2]. Initially, CV stage is used to charge the lead-acid battery, which aims to avoid the electrolysis of the water at the end of the charge, and hence, to prevent excessive gaseous emissions [26]. As we know, both the component material and electrochemical mechanism of the lithium-ion battery is apparently different from that of the lead-acid battery; thus, we are going to study whether the CV stage is necessary for the lithium-ion battery charging.

First, the contributions of CV stage to the battery are studied, then the CC/CV strategy is compared with the CC strategy, and three evaluation criterions, including the charging time, the charging capacity and the charging energy efficiency, are adopted in order to evaluate them. The specific parameters of the test battery are listed in Table 1.

**Table 1.** Specific parameters of test battery.

Parameter	Value	Parameters	Materials	Thickness
Rated voltage	3.2 V	Anode plate	aluminum	19 $\mu\text{m}$
Voltage lower limit	2.5 V	Anode material	LiFePO <sub>4</sub>	35 $\mu\text{m}$
Voltage upper limit	3.8 V	Separator	PP/PE/PP	40 $\mu\text{m}$
Nominal capacity	8 AH	Cathode material	Graphite	40 $\mu\text{m}$
Current limit (discharge)	30 A	Cathode plate	Copper	11 $\mu\text{m}$
Temperature (charge)	0~45 °C	Shell	Aluminum	500 $\mu\text{m}$
Temperature (discharge)	-20~45 °C			
Resistance	2.5 m $\Omega$			
Weight	900 g			
Dimension	135 mm $\times$ 70 mm $\times$ 80 mm			
Layers	63			

The charging current rates and temperatures often affect the battery characteristics, for they influence the electrochemical reaction speed; thus, we consider their effects on the three criteria in the following experiments. The charging and discharging equipment is MACCOR model 4300 (MACCOR, Tulsa, OK, USA), and the thermostatic equipment is Votsch C4-180 (Vötsch Industrietechnik, Stuttgart, Germany). The experimental procedures are elaborated as follows:

(1) Capacity and resistance calibration:

Six batteries in the same batch are selected, and their capacities and resistances are calibrated to make sure that their characteristics are almost the same. They, in turn, are numbered as No.1, No.2, No.3, No.4, No.5 and No.6, and each of them is discharged with 1 C (current rate) until it reaches minimum allowed voltage (2.5 V).

(2) Different charging current rate tests for CV stage

Set the temperature in the Votsch C4-180 to be 30 °C, and the CC/CV strategy is used to charge battery No.1. First, CC charging is applied at 0.5 current rate (4 A) until its voltage reaches the cut-off value (3.65 V). Then, the CV charging begins, the battery current decreases until it reaches below 0.01 current rate (0.08 A). The charging times and charging capacities of CV stage and the whole process can be shown by MACCOR model 4300. After recording the raw experimental data, the battery No.1 needs to be fully discharged with 1 current rate (8 A), then we repeat the experimental processes above, but only change the charging current in the CC stage to 1 current rate (8 A), 1.5 current rate (12 A), 2 current rate (16 A) as well as 2.5 current rate (20 A), respectively.

(3) Different temperature tests for CV stage

CC/CV strategy is used to charge battery No.2, but not in the same way outlined above in (2). The CC charging current is unchanged, which is set as 1 current rate (8 A). Instead, the charging tests under different temperatures (−10, 10, 30 and 50 °C) are considered, and the other test conditions are the same as those in (2).

(4) Different charging current rate tests for the charging time and charging capacity comparison between CC and CC/CV strategy

Set the temperature in the Votsch C4-180 to be 30 °C, CC strategy is used to charge battery No.3, and CC/CV strategy is used to charge battery No.4. In CC strategy, CC charging is applied at 0.5 current rate (4 A) until its voltage reaches the cut-off value (3.65 V), then the charging process is over. In CC/CV charging, battery No.4 is first charged with a constant current rate (0.5A) until its voltage reaches 3.65 V, then the CV stage begins, and the battery current decreases until it goes below 0.01 current rate (0.08 A). After recording the experimental data, the tests should be repeated under different charging current rates (1 current rate (8 A), 1.5 current rate (12 A), 2 current rate (16 A) as well as 2.5 current rate (20 A)).

(5) Different temperature tests for the charging time and charging capacity comparison between CC and CC/CV strategy

The test contents are similar to those in (4), but the charging current rate is fixed as 1 current rate (8 A), and the test temperatures are −10, 10, 30 and 50 °C, respectively.

(6) Different charging current rate and temperature tests for the charging energy efficiency comparison between CC and CC/CV strategy

Set the temperature in the Votsch C4-180 to be 30 °C, CC strategy is used to charge battery No.5, and CC/CV strategy is used to charge battery No.6, and the charging energy efficiencies of CC strategy and CC/CV strategy are recorded under different charging current rates (0.5 current rate (4 A), 1 current rate (8 A), 1.5 current rate (12 A), 2 current rate (16 A) as well as 2.5 current rate (20 A)). Then, the charging current rate is set to be unchanged, which is 1 current rate (8 A), and the charging energy efficiencies of CC strategy and CC/CV strategy are recorded under different test temperatures (−10, 10, 30 and 50 °C).

In Figures 1 and 2, the blue coordinate represents the ratio between the capacity charged in the CV stage and that charged in the whole CC/CV process, and the red coordinate shows the time taken by the CV stage and that taken by the whole CC/CV process. Figure 1 shows that the bigger the charging rate, the bigger the time percentage and capacity percentage in the CV stage, but the increments of time percentages are far greater than that of the capacity. Figure 2 shows that the higher the temperature, the smaller the time percentage and capacity percentage in the CV stage, but the decrements of time

percentages are far greater than that of the capacity. In summary, they indicate that the CV stage takes much charging time, but with less energy charging into the battery.

Then, we further compare the characteristics of CC strategy and CC/CV strategy based on the charging time, the charging capacity as well as the charging energy efficiency. It is worth mentioning that the cut-off voltage should be the same in the two charging strategies. In Figure 3, the blue curve represents the ratio between the time taken by CC strategy and that taken by CC/CV strategy, and the red curve represents the ratio between the capacity charged in CC strategy and that charged in CC/CV strategy. It clearly shows that the total capacity charged in the CC strategy is almost identical to that charged in the CC/CV strategy, and the ratio between them is higher than 96% despite different charging rates. Additionally, the charging time taken by the CC strategy is much smaller than that taken by the CC/CV strategy, especially under high charging rate conditions.

Another two batteries in the same batch are used to test the same contents in Figure 3, but with different temperatures, as shown in Figure 4. It shows that the capacity charged in CC strategy is nearly the same as that charged in CC/CV strategy when at a high temperature range. At low temperatures, the charging capacity differences between CC strategy and CC/CV strategy become obvious due to the slower electrochemical reaction speed. Thus, the CV stage is necessary for the battery charging at low temperatures, but it takes an extremely long time. Fortunately, charging at low temperatures does not happen too often in practice.

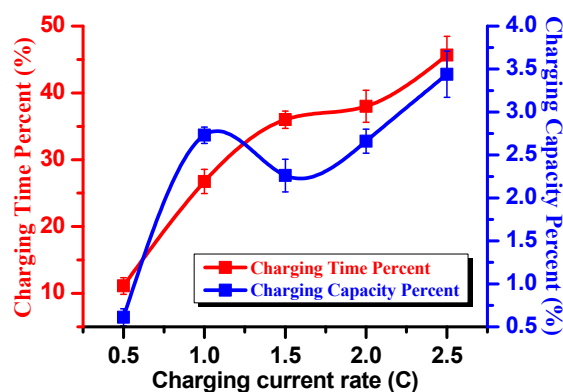


**Figure 1.** Charging capacity percentage and charging time percentage of CV stage in CC/CV (constant current/constant voltage) strategy at different charging current rates.

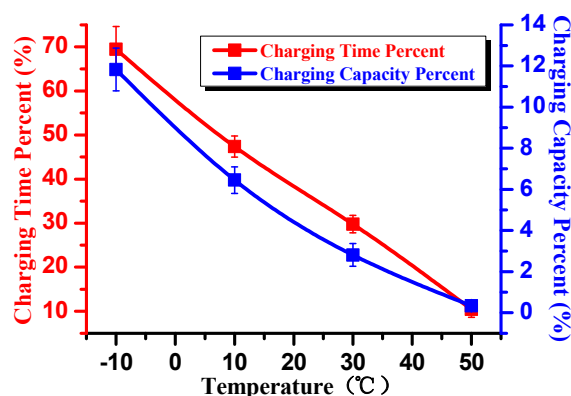


**Figure 2.** Charging capacity percentage and charging time percentage of CV stage in CC/CV strategy at different temperatures.

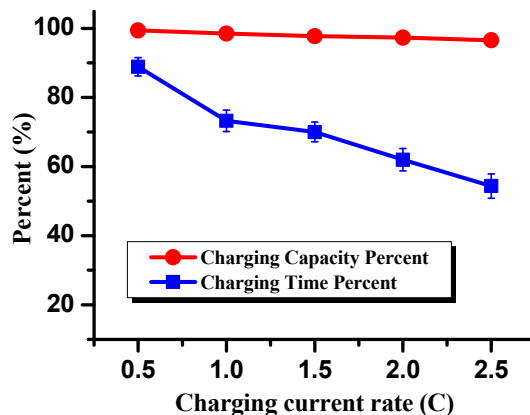


**Figure 3.** Charging time percentage and charging capacity percentage between CC strategy and CC/CV strategy at different charging current rates.

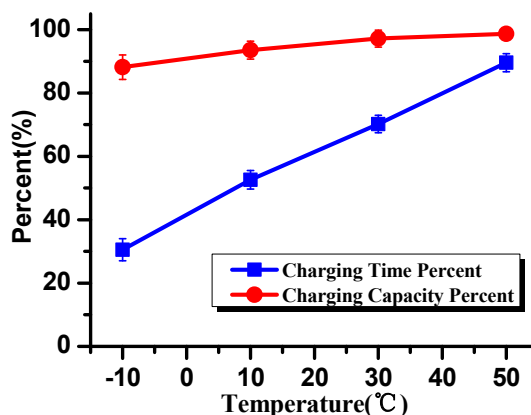


**Figure 4.** Charging time percentage and charging capacity percentage between CC strategy and CC/CV strategy at different temperatures.

Subsequently, the charging energy efficiencies between CC strategy and CC/CV strategy are compared at different charging current rates and temperatures, and the results are shown in Figures 5 and 6. Both indicate that the charging energy efficiency of CC strategy is always higher than that of CC/CV strategy despite different charging rates and temperatures. Additionally, CC strategy can slow down the capacity fading of the batteries compared to the CC/CV strategy [27]. Thus, we can deduce that CC strategy is superior to CC/CV strategy, and thus is more suitable for battery wireless charging.

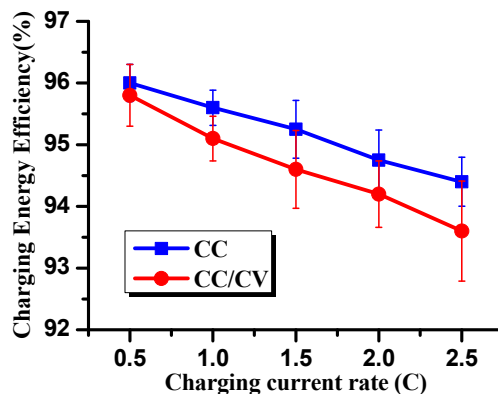


**Figure 5.** Charging energy efficiencies of CC strategy and CC/CV strategy at different charging current rates.

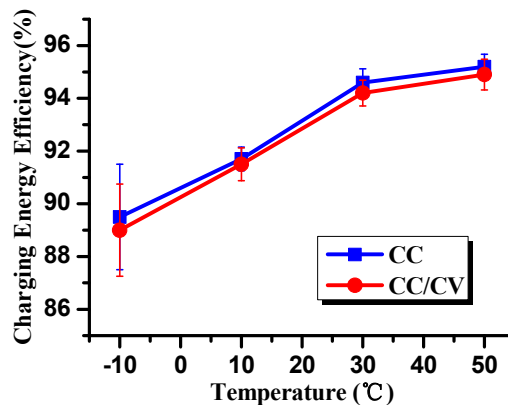


Figure 6. Charging energy efficiencies of CC strategy and CC/CV strategy at different temperatures.

### 3. State Space Model of the Receiver

A typical wireless charging system, including the PFC (power factor correction), the H Bridge, the resonant topology, the rectifier, the DC/DC and the load, is shown in Figure 7.

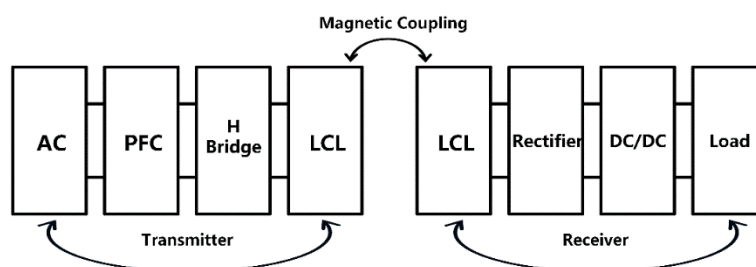


Figure 7. Schematic of wireless charging system, AC represents the 220 V alternating current power grid, PFC (power factor correction) is normally a boost converter, LCL is a kind of resonant topology and DC/DC is used to regulate the transfer power.

In this paper, a LCL-LCL topology is adopted. Because the LCL topology is a variant derived from LC parallel topology, it has a CC characteristic; thus, the transmitter can produce a sine current with a constant amplitude despite different magnetic coupling conditions, and the receiver can also produce an unchanged charging current for the battery. In this case, the DC/DC part is useless, for the CC charging function is substituted by the LCL topology, and the power regulation function is substituted by the H Bridge. Thus, we can remove the DC/DC part, and it is beneficial to improve the transfer efficiency, because the power MOSFETs in the DC/DC part will induce additional switching losses. Then, the schematic shown in Figure 7 can be simplified as Figure 8.

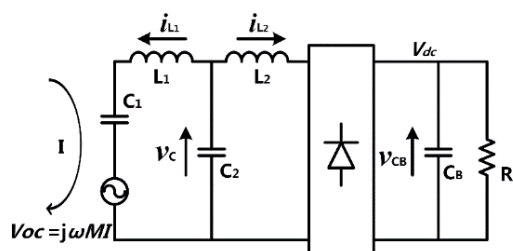


Figure 8. Simplified equivalent circuit of the receiver.

Where  $I$  represents the current produced by the transmitter,  $M$  represents the mutual inductance between the two magnetic coils of the transmitter and receiver,  $\omega$  is the system operating frequency, and  $V_{OC}$  is the transmitted voltage from the transmitter to the receiver.  $L_1$  is the magnetic coil that couples with transmitter through the magnetic field,  $C_2$  is the resonant capacitor, and  $L_2$  is the matching inductor of  $L_1$ , which makes the reflected impedance from the receiver to the transmitter purely resistive. Because the receiver should be mounted on the vehicle chassis, the height of the magnetic coils  $L_1$  should be far smaller than the distance between the ground and chassis. Obviously, the helix coil is not appropriate, and thus the magnetic coil  $L_1$  is designed to be a spiral coil. As we know, the bigger the coupling coefficient, the higher the transfer efficiency, so the magnetic coil  $L_1$  is usually bulky to pursue a big coupling coefficient, and this leads to a bulky matching inductor  $L_2$ , since their inductances must be identical. With the purpose of reducing the volume and weight of the matching inductor  $L_2$ , we add an additional compensating capacitor  $C_1$ , and the equivalent inductance of  $L_1$  and  $C_1$  should be the same as that of  $L_2$ . Additionally,  $C_B$  is a filter capacitor and  $R_L$  is the load.

A state space model is introduced to analyze the system dynamic characteristics. First, we should select the appropriate state variables. Although the state variables are diverse, which include physical variables, phase variables, canonical variables and so on, the physical state variables are used in this paper, as they can directly describe the system characteristics. So, we have

$$\begin{cases} x_1(t) = v_c(t) \\ x_2(t) = i_{L_1}(t) \\ x_3(t) = i_{L_2}(t) \\ x_4(t) = v_{C_B}(t) \end{cases} \quad (1)$$

where  $v_c(t)$ ,  $i_{L_1}(t)$ ,  $i_{L_2}(t)$  and  $v_{C_B}(t)$  represent the voltage across the resonant capacitor  $C_2$ , the current flowing through the inductor  $L_1$ , the current flowing through the inductor  $L_2$  and the voltage across the capacitor  $C_B$ , respectively. According to KVL, the differential equations can be written as

$$\begin{cases} i_{L_1} + i_{L_2} + C_2 \frac{dv_c}{dt} = 0 \\ L_2 \frac{di_{L_1}}{dt} + V_{OC} - v_c = 0 \\ L_2 \frac{di_{L_2}}{dt} \pm v_{C_B} - v_c = 0 \\ -|i_{L_2}| + C_B \frac{dv_{C_B}}{dt} + \frac{v_{C_B}}{R_L} = 0 \end{cases} \quad (2)$$

where the voltage  $V_{dc}$  across the capacitor  $C_B$  is assumed to be constant, and the forward voltages of the four diode are neglected. Normally, the forward voltage of the power diode is around 0.7 V, and the voltage level of the battery pack for electric vehicles is around 300 V, which is far greater than 0.8 V. In the state space model, the equivalence simplification between the AC side and the DC side is very important. The sinusoidal current  $i_{L_2}(t)$  in the AC side changes to a positive half-sine-wave current ( $|i_{L_2}(t)|$ ) after flowing through the rectifier. Additionally, the DC voltage  $v_{C_B}(t)$  in the DC side is



equivalent to a quasi-square-wave voltage ( $\pm v_{C_2}(t)$ ) in the AC side. Then, the state space model can be written as

$$\begin{cases} \begin{bmatrix} \dot{x}_1 \\ \dot{x}_2 \\ \dot{x}_3 \\ \dot{x}_4 \end{bmatrix} = \begin{bmatrix} 0 & -1/C_2 & -1/C_2 & 0 \\ 1/L_2 & 0 & 0 & 0 \\ 1/L_2 & 0 & 0 & \pm 1/L_2 \\ 0 & 0 & \pm 1/C_B & -1/R_L C_B \end{bmatrix} \begin{bmatrix} x_1 \\ x_2 \\ x_3 \\ x_4 \end{bmatrix} + \begin{bmatrix} 0 \\ -1/L_2 \\ 0 \\ 0 \end{bmatrix} V_{oc} \\ \begin{bmatrix} y_1 \\ y_2 \end{bmatrix} = \begin{bmatrix} 0 & 0 & 1 & 0 \\ 1 & 0 & 0 & 0 \end{bmatrix} \begin{bmatrix} x_1 \\ x_2 \\ x_3 \\ x_4 \end{bmatrix} \end{cases} \quad (3)$$

For battery charging, the load  $R_L$  should be substituted by a voltage source  $V_B$  as well as its internal resistance  $R_B$ , and the differential equations should be rewritten as

$$\begin{cases} i_{L_1} + i_{L_2} + C_2 \frac{dv_c}{dt} = 0 \\ L_2 \frac{di_{L_1}}{dt} + V_{oc} - v_c = 0 \\ L_2 \frac{di_{L_2}}{dt} \pm (I_c \cdot R_B + V_B) - v_c = 0 \\ -|i_{L_2}| + R_B C_B \frac{dI_c}{dt} + I_c = 0 \end{cases} \quad (4)$$

where  $I_c$  is another state variable which represents the charging current for the battery. Table 2 shows the specific parameters used in the state space model.

**Table 2.** Specific parameters in the state space model.

Parameter	Value
Magnetic coil $L_1$	164.5 $\mu$ H
Mutual inductance $M$	64 $\mu$ H
Transfer distance $D$	20 cm
Operating frequency $f$	80 kHz
Matching inductor $L_2$	40 $\mu$ H
Compensating capacitor $C_1$	31.82 nF
Resonant capacitor $C_2$	99.05 nF
Filter capacitor $C_B$	160 $\mu$ F
Battery pack voltage $V_B$	300 V
Internal resistance $R_B$	0.8 m $\Omega$

The current produced by the transmitter is around 10 A, which can be regulated by the phase shifting control of the H Bridge. Substitute these parameters into Equation (4), we can have the state space model as shown in Figure 9.

Based on the state space model, we can analyze the system dynamic characteristics as shown in Figure 10. It clearly shows that  $i_{L_1}(t)$  lags 90 degrees behind  $i_{L_2}(t)$ , which shows a good agreement with the theoretical result [28], and there are some superimposed ripples on the charging current  $I_C$ .

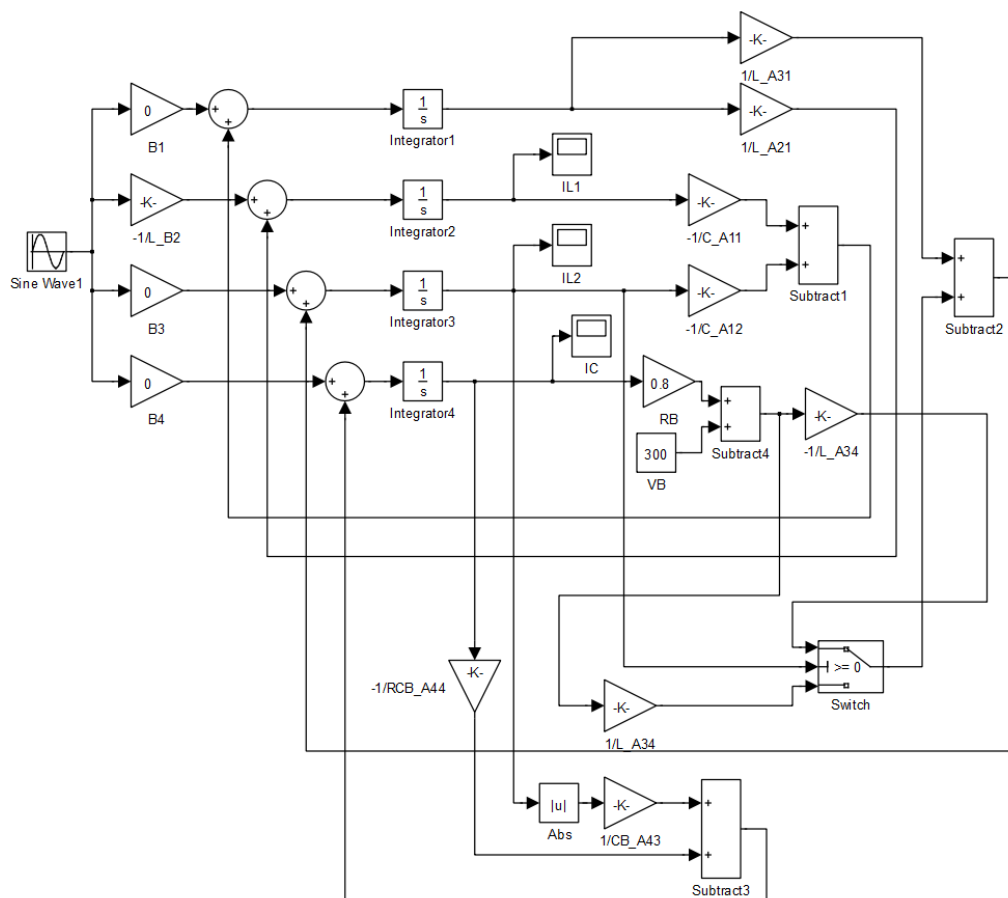


Figure 9. State space model based on the equivalent circuit.

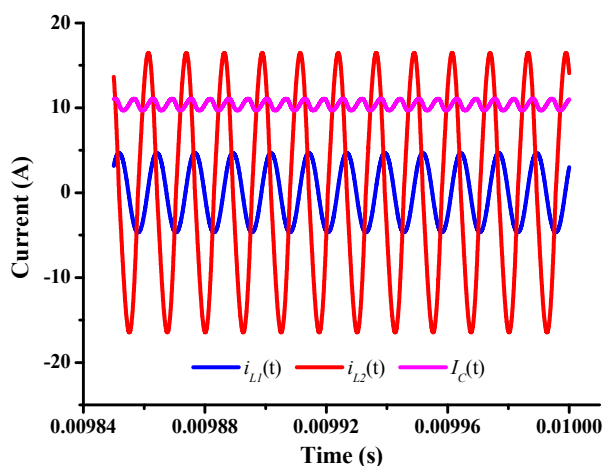


Figure 10. Dynamic characteristics of the currents in the receiver.

As we know, the filter capacitors are necessary for the traditional charger design, since the load requires a rated voltage to work, and the ripple currents or voltages must be limited under the pre-designed value. However, the design may be different for the battery wireless charging. As the power

battery has a strong voltage source characteristic and the LCL-LCL topology has a CC charging characteristic, the filter capacitors can be reduced or even removed. These can reduce the volume and weight of the receiver, which are helpful to improve the system power density. By reducing or removing the filter capacitor  $C_B$  in Equation (4), we can have the state space models under different situations. Figure 11 shows the charging currents for the battery when the filter capacitor takes different values. It clearly shows that the smaller the filter capacitor, the bigger the ripple current. When there is no filter capacitor, the charging current becomes a sinusoidal half-wave current.

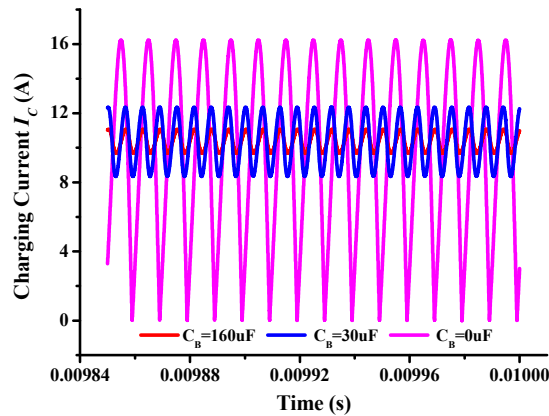


Figure 11. Charging currents with different filter capacitors.

#### 4. Rationality Validation of Nonuse Filter Capacitor

We should guarantee that the transfer characteristics are unchanged when the filter capacitors are reduced or removed. Figure 12 shows the system transfer characteristics with different output filter capacitors, where the input voltage is 400 V, the battery voltage is set to 300 V. The coupling coefficients at 15 and 20 cm transfer distances are 0.4585 and 0.364, respectively. We can find that the transfer characteristics at two different transfer distances are almost unchanged although the filter capacitors are different, which indicates that the nonuse or reduction design of the output filter capacitors has no effects on system transfer characteristics, only increases the current ripples.

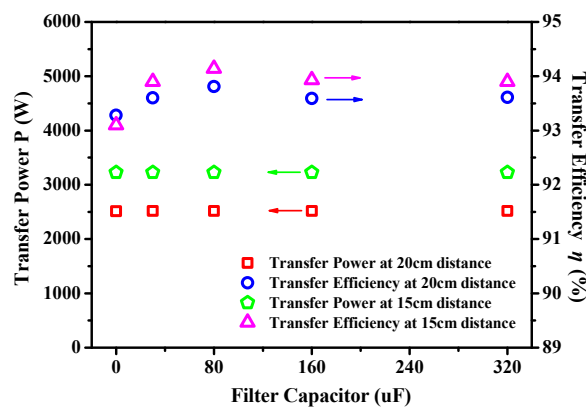
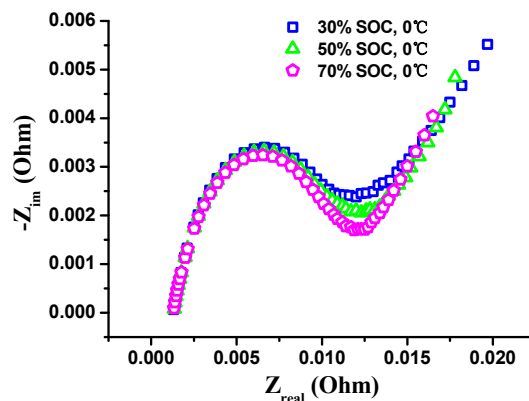


Figure 12. System transfer characteristics with different output filter capacitors.

Although we have already validated that the nonuse of the filter capacitor has no effects on the system transfer characteristics, we still do not know whether the output filter capacitor has protective effects on

the battery. Thus, an electrochemical analysis method named EIS is introduced, which is a frequency domain method to analyze electrochemical processes occurring at electrode/electrolyte interfaces. By analyzing the EIS curves of the battery, we can study the internal electrochemical mechanisms of the battery, and verify our assumption fundamentally.

Generally, EIS curves are easily affected by temperatures or SOC (state of charges), Figures 13–15 show the EIS curves at different SOC when the temperatures are 0, 23 and 45 °C, and they clearly show that our test batteries are not sensitive to SOC, thus this paper only considers the effects caused by different temperatures (0, 20 and 40 °C).



**Figure 13.** Electrochemical impedance spectrum (EIS) curves at different state of charges (SOCs) when the test temperature is 0 °C.

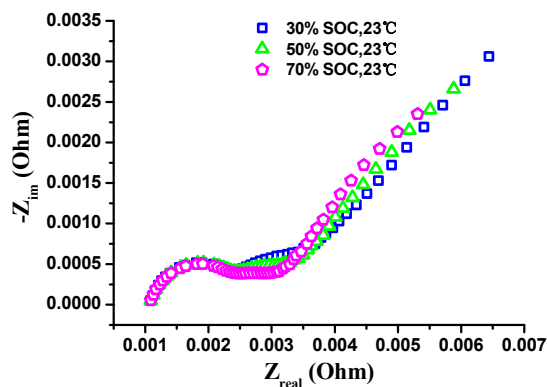


**Figure 14.** EIS curves at different SOC when the test temperature is 23 °C.

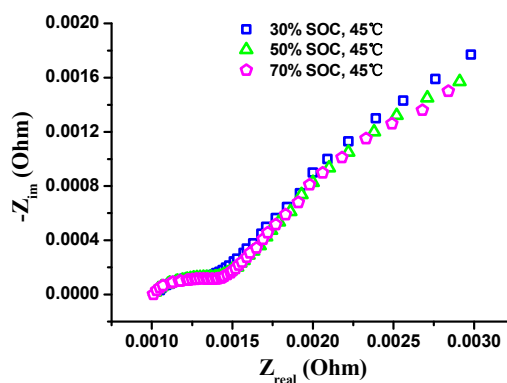


**Figure 15.** EIS curves at different SOC when the test temperature is 45 °C.

First, we select two batteries in the same batch; one is paralleled with nothing; and the other is paralleled with an aluminum electrolytic capacitor; the specific parameters of which are listed as  $470 \mu\text{F}/450 \text{ V}/-25\sim 105 \text{ }^\circ\text{C}/\Phi 35 \times 45 \text{ mm}$ . Then, we test the EIS curves of the battery and that with a parallel capacitor, respectively, where the EIS equipments are solartron SI 1287 Electrochemical interface, solartron 1255B frequency response analyzer and TOYO corporation (Akanehama, Japan) model PBI250-10 Power Booster. The test temperature is controlled by the thermostatic equipment Votsch C4-180, and the test results are shown in Figure 16. EIS curve is actually a Nyquist plot, which shows the complex impedance in a single curve over the entire frequency range. As the battery characteristics are mainly capacitive, the sign of the imaginary axes is reversed to bring the curve into the upper part of the diagram. Apparently, we can find that the EIS curves of the battery and that with a parallel capacitor are almost the same when the test temperatures are 20 and 40  $^\circ\text{C}$ , which means that their electrochemical characteristics in these two situations are similar; hence, we deduce that the parallel capacitor may have no good effects on the battery characteristics. There are little differences in the high frequency part when the test temperature is 40  $^\circ\text{C}$ ; they are caused by the lead wire inductance of the parallel capacitor; since the test frequencies in this part are higher than 1 kHz. When the test temperature reduces to 0  $^\circ\text{C}$ , the differences between them become more and more apparent as the battery impedance characteristics at low temperatures are really poor and very sensitive to temperatures. There are two possibilities: First, the difference is caused by the errors of test temperature because the temperature precision of the thermostatic equipment used is 1  $^\circ\text{C}$ . Second, indeed, the parallel capacitor plays a part in the electrochemical process. However, charging at 0  $^\circ\text{C}$  temperature does not happen too often in practice.

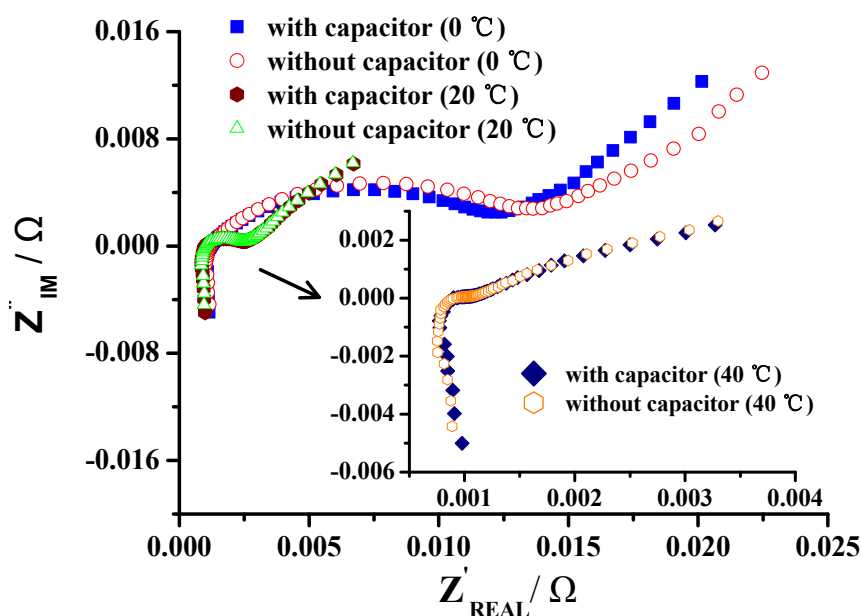


**Figure 16.** EIS curves of the battery with and without capacitor at 0, 20 and 40  $^\circ\text{C}$ .

Then, the internal polarization process is described based on EIS curve, and the correspondences are shown in Figure 17. EIS curves are comprised of the inductive tail at high frequencies, which is ascribed to the parasitic inductances of lead wires; the intersection on the real axis which represents the total ohmic resistance of the battery; the semicircle in mid-frequency range which is characteristic of the

charge transfer at the electrode/electrolyte interface and the electrochemical double layer; the oblique (it can be called the mass-transfer area) at low frequencies which represents the solid-state Warburg diffusion of lithium ions [29]. For the frequencies lower than 10 Hz, the solid-state Warburg diffusion phenomenon of lithium ions is dominant, since it has time to be established. However, for the frequencies from 10–460 Hz, the reactions of diffusion do not have time to be carried out, thus the phenomenon of charger-transfer becomes dominant [26]. When the frequencies are higher than 460 Hz, the EIS curves cannot reflect the battery electrochemical characteristics, since the effects caused by the battery lead wires are dominant. Obviously, the mass transport part (lower than 10 Hz) and the charge transfer part (from 10–460 Hz) are the battery polarization process. When the frequencies are higher than 460 Hz, the polarization process does not happen, thus the power signals in this case have no effects on the battery characteristics. SAE J2954 (works in progress) suggests that the operating frequency of wireless charging system for electric vehicles should range from 80–90 kHz, thus 80 kHz is selected as the system operating frequency in this paper. In this situation, the first harmonic frequency of the charging current is 160 kHz, which is far greater than 460 Hz. It indicates that the sinusoidal half-wave charging currents caused by the nonuse output filter capacitors do not affect the battery polarization process, and hence, the battery characteristics only cause a little heat loss in the ohmic resistance of the battery.

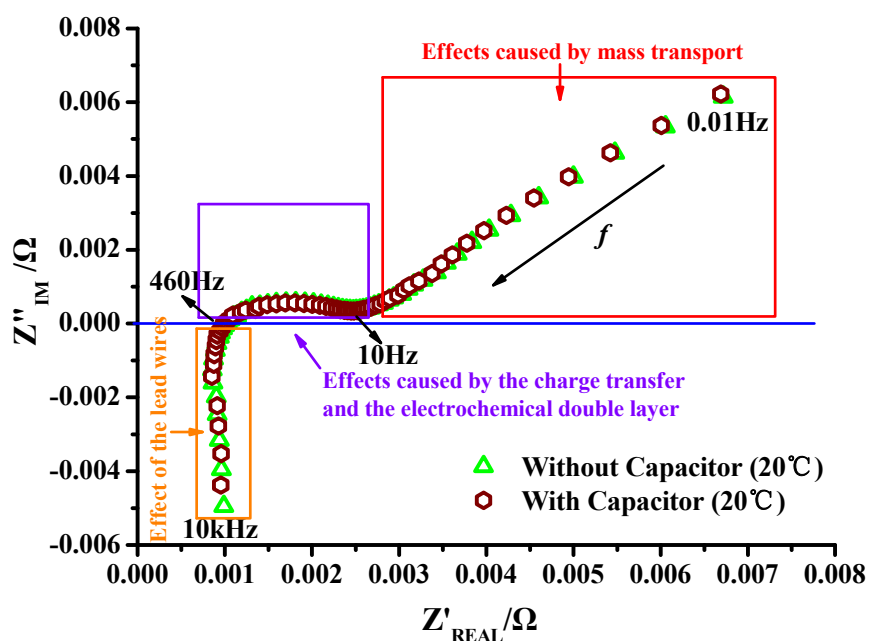


**Figure 17.** Correspondences between EIS curve and internal polarization process.

Figure 18 shows the deterioration curves of the battery charged by SRC (sinusoidal ripple current charge) and CC-CV [30], and this phenomenon is helpful to validate our assumption although the harmonic components of the charging current with no filter capacitors are bigger than those used in SRC. It clearly shows that the Lithium-ion battery capacities charged by SRC and CC-CV deteriorate to 93.4% and 89.9% after 1000 cycles, respectively, which indicates that the battery lifetime is improved with SRC. It is interesting that the nonuse of the filter capacitor may be beneficial to extend the battery lifetime.

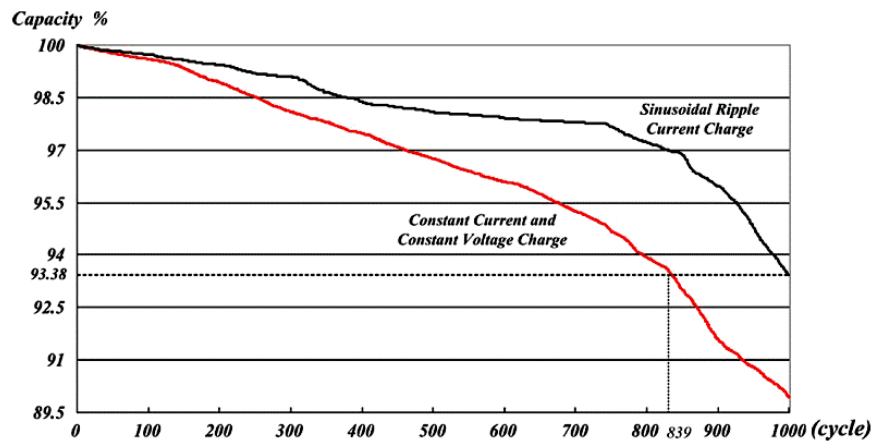


**Figure 18.** Deterioration curves charged by sinusoidal-ripple-current charge (SRC) and CC-CV.

## 5. Experimental Section

A prototype is fabricated to validate our research results as shown in Figure 19, which includes the input power source, the H Bridge, two magnetic coils, the rectifier as well as the battery pack. The power source is Chroma 62100H-600 high-voltage DC power supply, and its operating range is 600 V/17 A/10 kW. The battery pack consists of 24 pieces of “sail” lead-acid battery instead of lithium-ion battery, since the lithium-ion battery may rupture, ignite or even exploded while overcharging [31]. The comparison between CC strategy and CC/CV strategy as well as EIS tests have already been done based on single lithium-ion battery, thus the lead-acid battery pack is only employed to verify the charging characteristics when there are no filter capacitors. The magnetic coils are optimized based on the finite element software, but the optimization flow are not demonstrated due to the space limit.



**Figure 19.** A prototype of a wireless charging system.

The following results are measured by Tektronix DPO 3054 (Tektronix, Beaverton, OR, USA), the current probe is Tektronix TCP0020, and the high voltage probe is Tektronix P5201. The filter capacitors used in this paper are EPCOS B32776 and B32778 series. Figure 20 shows some critical waveforms of the prototype when there is no filter capacitor in the receiver. The cyan curve is the output voltage produced by H Bridge. Because the reduction scale of the high voltage probe is 200, the measured voltages need to be multiplied by 200. The green curve shows the dynamic current which flows through the inductor  $L_2$  in Figure 8. The purple curve is the charging current for the battery pack, which shows a

good agreement with the theoretical results in Figure 11, and it is a sinusoidal half-wave current since the filter capacitor is removed. If we keep its average value as 10.3 A, the charging power requirement can be still satisfied.

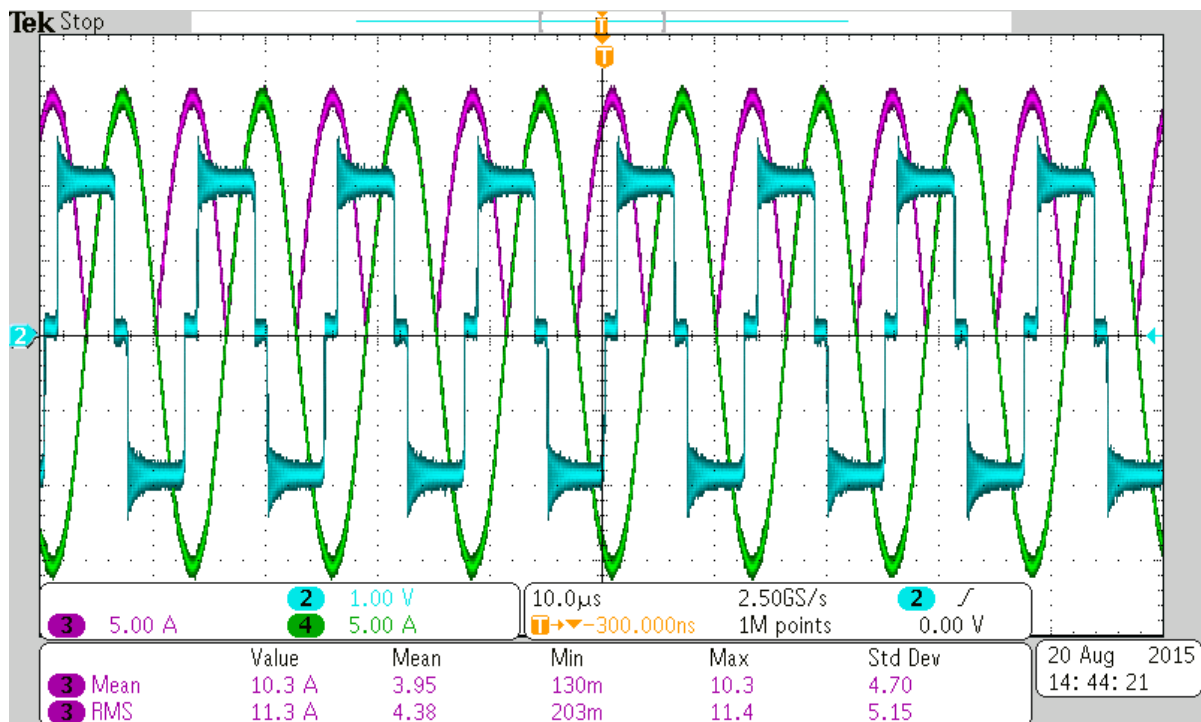


**Figure 20.** Critical waveforms when there is no filter capacitor in the receiver.

Figure 21 shows the dynamic charging currents as well as the currents flowing through the inductor  $L_2$  in Figure 8 when the filter capacitors are 30, 80, 160 and 320  $\mu\text{F}$ , respectively. We can clearly find that the averages of the charging currents are the same when the filter capacitors are different, but the current ripples are different. The bigger the filter capacitor, the smaller the current ripples. As shown in Figure 21a, when the filter capacitor is 30  $\mu\text{F}$ , the charging current ripples are different from those shown in Figure 11. This is mainly because an additional diode is inserted between the filter capacitor  $C_B$  and the battery  $V_B$  in practice, which is used to prevent the battery to charge the filter capacitor reversely. However, in the theoretical model, the current between the filter capacitor  $C_B$  and the battery  $V_B$  is bidirectional. Although the ripple currents shown in Figure 21a are different from those shown in Figure 11, their amplitudes are the same, which are all 2 A. With the increase of the filter capacitor, the charging current ripples become the sine waves basically, and the ripples are almost unchanged when the filter capacitor is bigger than 160  $\mu\text{F}$ .

Then, we will compare the system transfer characteristics when the filter capacitors are different. As shown in Figure 22, the system transfers the same power despite different filter capacitors, and this can also be found in Figures 20 and 21, for the charging currents are the same (10.4 A). Also, they show a good agreement with the simulations in Figure 12. However, the experimental transfer efficiencies are a little lower than those shown in Figure 12. In practice, we cannot make the values of the resonate and compensating capacitors the same as those used in the simulation, and thus the system may not be in the quasi-resonant state, which lowers the system transfer characteristics. Additionally, the current probe TCP0020 is a hall device, and thus there are certain measure errors in the test currents, which could also



cause the drop in efficiency. With the increase of the filter capacitors, we can find that the efficiency takes on a slightly increasing trend. However, such a small difference can be ignored in practice.

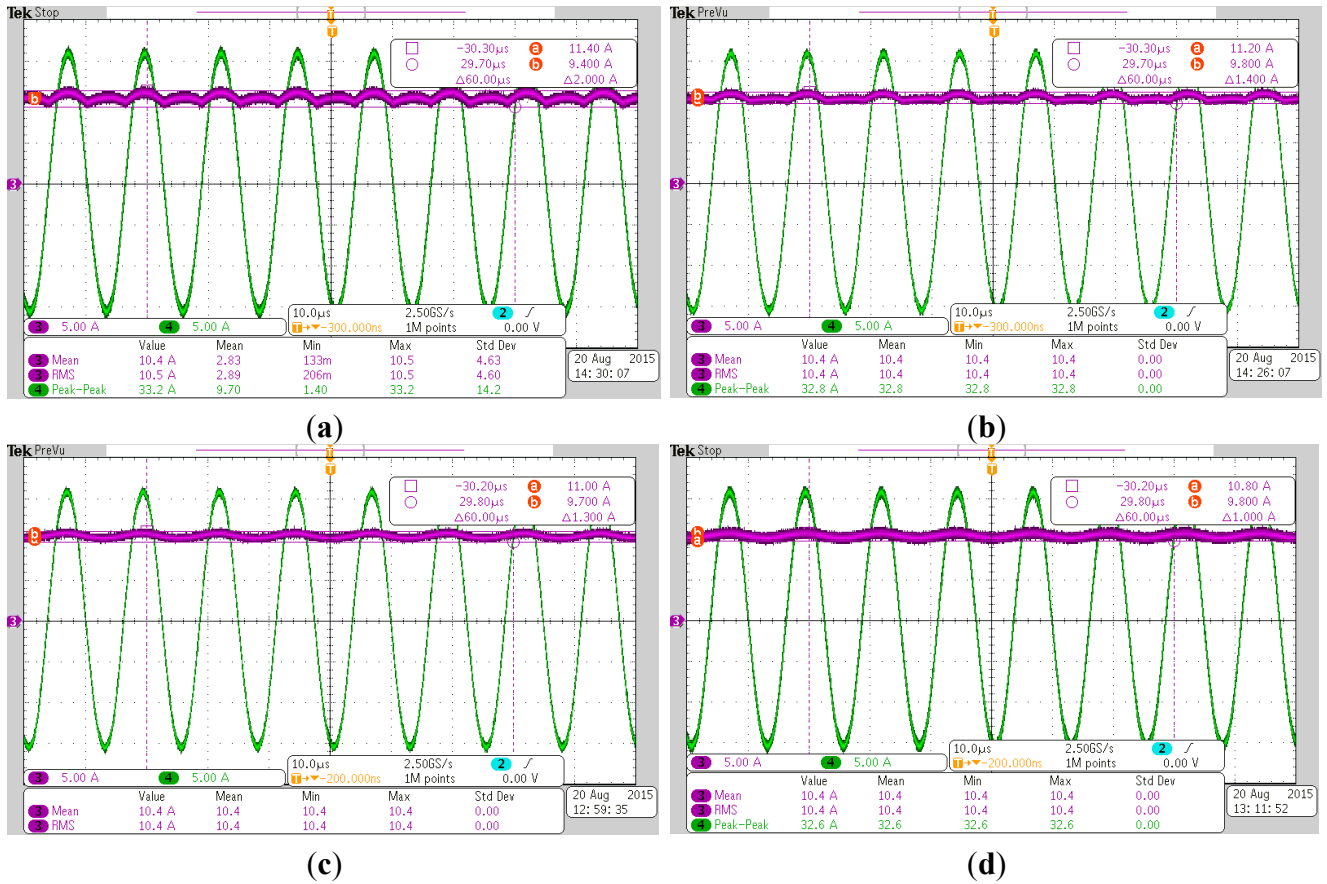


Figure 21. Critical waveforms when the filter capacitors are (a) 30, (b) 80, (c) 160 and (d) 320  $\mu\text{F}$ .

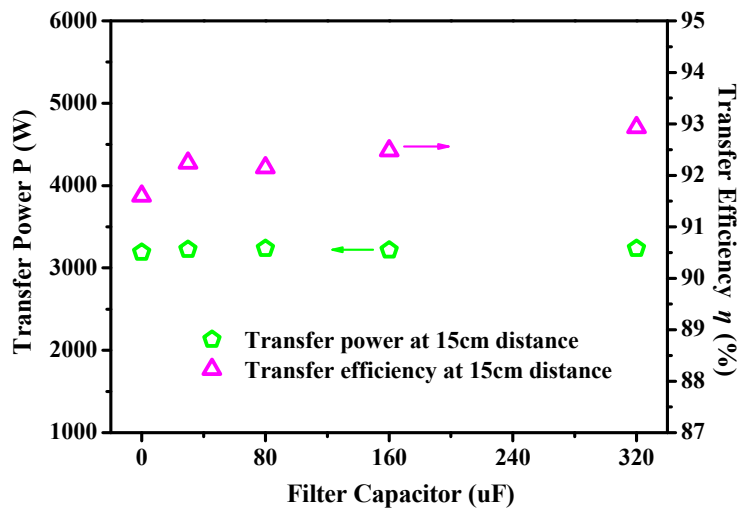
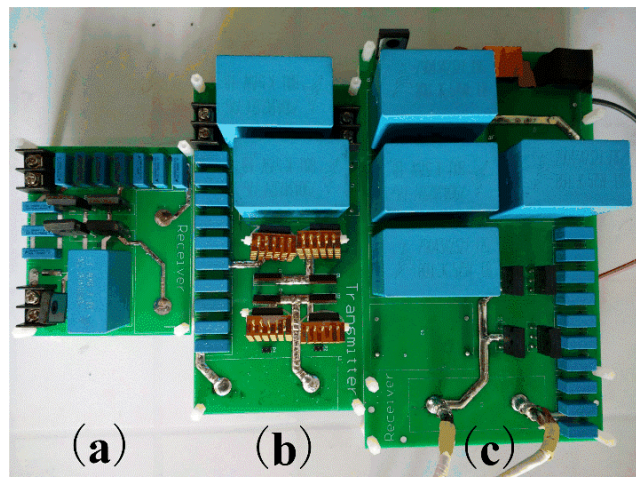


Figure 22. System transfer characteristics with different filter capacitors at 15 cm distance.

We have already validated that the system transfer characteristics are almost unchanged although the filter capacitors are different, and it is beneficial to the miniaturization and lightweight design of the receiver. Figure 23 shows three receiver boards with different filter capacitors: the left one has a 30  $\mu\text{F}$  filter capacitor, the middle one has two 80  $\mu\text{F}$  filter capacitors, and the left one has four 80  $\mu\text{F}$  filter

capacitors. Apparently, the left board is smaller and lighter than the other two boards. Normally, the receiver board is mounted on the vehicle chassis; for that, the smaller and lighter it is, the better. If the 30  $\mu\text{F}$  filter capacitor of the left receiver board in Figure 23 is removed, the volume and weight of the board can be further reduced. This is beneficial to the design of wireless charging systems for electric vehicles.



**Figure 23.** Receiver board with the 30  $\mu\text{F}$  (a), 160  $\mu\text{F}$  (b) and 320  $\mu\text{F}$  (c) filter capacitors.

## 6. Conclusions

Some design considerations are studied in this paper. First, the CC strategy is compared with the CC/CV strategy based on three criteria, including the charging time, the charging capacity and the charging energy efficiency. Experiments show that the CV stage takes most of the charging time, but with less energy charging into the battery, and the effective charging capacities of the two strategies are almost the same, but the charging energy efficiency of the CC strategy is a little higher than that of the CC/CV strategy. Then, a state space model for the receiver is built to study the variations of charging current when the output filter capacitors are different, and a new receiver design without output filter capacitors is proposed, which helps to improve the system power density and avoid the drop in efficiency caused by capacitor degradation. At last, we test the EIS curves of two batteries at different temperatures; one is paralleled with an electrolytic capacitor, and the other is not. The results show that the capacitor paralleled with the battery has no good effects on the battery characteristics. Additionally, the electrochemical mechanisms of the battery are elaborated based on the EIS curve, and we find that the polarization process has no time to be established when the frequency is higher than 460 Hz. Thus, the sinusoidal half-wave charging currents caused by nonuse output filter capacitors do not affect the battery characteristics if their frequencies are higher than 460 Hz. We hope our work is beneficial to the research of wireless power transfer.

## Acknowledgments

The work was supported by the National High Technology Research and Development Program (“863” Program) of China (2011AA11A265). The manuscript was revised and improved by Haifeng Dai, and the authors appreciated his contributions.

## Author Contributions

Zhenshi Wang designed the system and analyzed the results, Xuezhe Wei provided guidance and key suggestions.

## Conflicts of Interest

The authors declare no conflict of interest.

## References

1. Li, X.H.; Zhang, H.R.; Peng, F.; Li, Y.; Yang, T.Y.; Wang, B.; Fang, D. A wireless magnetic resonance energy transfer system for micro implantable medical sensors. *Sensors* **2012**, *12*, 10292–10308.
2. Nair, V.V.; Choi, J.R. An integrated chip high-voltage power receiver for wireless biomedical implants. *Energies* **2015**, *8*, 5467–5487.
3. Kim, J.; Son, H.C.; Kim, D.H.; Park, Y.J. Optimal design of a wireless power transfer system with multiple self-resonators for an LED TV. *IEEE Trans. Consum. Electron.* **2012**, *58*, 775–780.
4. Xie, L.; Shi, Y.; Hou, Y.T.; Sherali, H.D. Making sensor networks immortal: An energy-renewal approach with wireless power transfer. *IEEE/ACM Trans. Netw.* **2012**, *20*, 1748–1761.
5. Covic, G.; Boys, J.T. Modern trends in inductive power transfer for transportation applications. *IEEE J. Emerg. Sel. Top. Power Electron.* **2013**, *1*, 28–41.
6. Wei, X.; Wang, Z.; Dai, H. A critical review of wireless power transfer via strongly coupled magnetic resonances. *Energies* **2014**, *7*, 4316–4341.
7. Kurs, A.; Karalis, A.; Moffatt, R.; Joannopoulos, J.D.; Fisher, P.; Soljačić, M. Wireless power transfer via strongly coupled magnetic resonances. *Science* **2007**, *317*, 83–86.
8. Duong, T.P.; Lee, J.W. A dynamically adaptable impedance-matching system for midrange wireless power transfer with misalignment. *Energies* **2015**, *8*, 7593–7617.
9. Sample, A.P.; Meyer, D.; Smith, J.R. Analysis, experimental results, and range adaptation of magnetically coupled resonators for wireless power transfer. *IEEE Trans. Ind. Electron.* **2011**, *58*, 544–554.
10. Ahn, D.; Hong, S. Effect of coupling between multiple transmitters or multiple receivers on wireless power transfer. *IEEE Trans. Ind. Electron.* **2013**, *60*, 2602–2613.
11. Keeling, N.; Covic, G.; Boys, J.T. A unity-power-factor IPT pickup for high-power applications. *IEEE Trans. Ind. Electron.* **2010**, *57*, 744–751.
12. Kiani, M.; Jow, U.M.; Ghovanloo, M. Design and optimization of a 3-coil inductive link for efficient wireless power transmission. *IEEE Trans. Biomed. Circuits Syst.* **2011**, *5*, 579–591.
13. Zaheer, A.; Covic, G.; Kacprzak, D. A bipolar pad in a 10-kHz 300-W distributed IPT system for AGV applications. *IEEE Trans. Ind. Electron.* **2014**, *61*, 3288–3301.
14. Shin, J.; Shin, S.; Kim, Y.; Ahn, S.; Lee, S.; Jung, G.; Jeon, S.; Cho, D. Design and implementation of shaped magnetic-resonance-based wireless power transfer system for roadway-powered moving electric vehicles. *IEEE Trans. Ind. Electron.* **2014**, *61*, 1179–1192.
15. Hwang, S.H.; Kang, C.G.; Son, Y.H.; Jang, B.J. Software-based wireless power transfer platform for various power control experiments. *Energies* **2015**, *8*, 7677–7689.

16. Wu, H.H.; Gilchrist, A.; Sealy, K.D.; Bronson, D. A high efficiency 5 kW inductive charger for EVs using dual side control. *IEEE Trans. Ind. Inform.* **2012**, *8*, 585–595.
17. Wang, B.; Yerazunis, W.; Teo, K.H. Wireless power transfer: Metamaterials and array of coupled resonators. *Proc. IEEE* **2013**, *101*, 1359–1368.
18. Puccetti, G.; Stevens, C.J.; Reggiani, U.; Sandrolini, L. Experimental and numerical investigation of termination impedance effects in wireless power transfer via metamaterial. *Energies* **2015**, *8*, 1882–1895.
19. Barré, A.; Suard, F.; Gérard, M.; Montaru, M.; Riu, D. Statistical analysis for understanding and predicting battery degradations in real-life electric vehicle use. *J. Power Sources* **2014**, *245*, 846–856.
20. Edström, K.; Gustafsson, T.; Thomas, J.O. The cathode-electrolyte interface in the Li-ion battery. *Electrochim. Acta* **2004**, *50*, 397–403.
21. Ceraolo, M. New dynamical models of lead-acid batteries. *IEEE Trans. Power Syst.* **2000**, *15*, 1184–1190.
22. Lee, S.; Choi, B.; Rim, C.T. Dynamics characterization of the inductive power transfer system for online electric vehicles by laplace phasor transform. *IEEE Trans. Power Electron.* **2013**, *28*, 5902–5909.
23. Wang, C.S.; Covic, G.; Stielau, O.H. Power transfer capability and bifurcation phenomena of loosely coupled inductive power transfer systems. *IEEE Trans. Ind. Electron.* **2004**, *51*, 148–157.
24. Boys, J.T.; Covic, G.; Xu, Y. DC analysis technique for inductive power transfer pick-ups. *IEEE Power Electron. Lett.* **2003**, *1*, 51–53.
25. Inoa, E.; Wang, J. PHEV charging strategies for maximized energy saving. *IEEE Trans. Veh. Technol.* **2011**, *60*, 2978–2986.
26. Lacrosonniere, F.; Cassoret, B.; Brudny, J.F. Influence of a charging current with a sinusoidal perturbation on the performance of a lead-acid battery. *IEE Proc. Electr. Power Appl.* **2005**, *152*, 1365–1370.
27. Monem, M.A.; Trad, K.; Omar, N.; Hegazy, O.; Mantels, B.; Mulder, G.; Van, P.; Van, J. Lithium-ion batteries: Evaluation study of different charging methodologies based on aging process. *Appl. Energy* **2015**, *152*, 143–155.
28. Thrimawithana, D.J.; Madawala, U.K. A generalized steady-state model for bidirectional IPT systems. *IEEE Trans. Power Electron.* **2013**, *28*, 4681–4689.
29. Gomez, J.; Nelson, R.; Kalu, E.E.; Weatherspoon, M.H.; Zheng, J.P. Equivalent circuit model parameters of a high-power Li-ion battery: Thermal and state of charge effects. *J. Power Sources* **2011**, *196*, 4826–4831.
30. Chen, L.R.; Wu, S.L.; Shieh, D.T.; Chen, T.R. Sinusoidal-ripple-current charging strategy and optimal charging frequency study for Li-ion batteries. *IEEE Trans. Ind. Electron.* **2013**, *60*, 88–97.
31. Ping, P.; Wang, Q.; Huang, P.; Li, K.; Sun, J.; Kong, D.; Chen, C. Study of the fire behavior of high-energy lithium-ion batteries with full-scale burning test. *J. Power Sources* **2015**, *285*, 80–89.